

Investigations of irradiation effects in crystalline and amorphous SiC

Cite as: J. Appl. Phys. **126**, 135902 (2019); doi: [10.1063/1.5085216](https://doi.org/10.1063/1.5085216)

Submitted: 10 December 2018 · Accepted: 28 August 2019 ·

Published Online: 4 October 2019



Benjamin J. Cowen,^{1,2,3}  Mohamed S. El-Genk,^{1,2,4,5,a)}  Khalid Hattar,³  and Samuel A. Briggs^{3,6} 

AFFILIATIONS

¹Institute for Space and Nuclear Power Studies, University of New Mexico, Albuquerque, New Mexico 87131, USA

²Nuclear Engineering Department, University of New Mexico, Albuquerque, New Mexico 87131, USA

³Sandia National Laboratories, Albuquerque, New Mexico 87185, USA

⁴Mechanical Engineering Department, University of New Mexico, Albuquerque, New Mexico 87131, USA

⁵Chemical and Biological Engineering Department, University of New Mexico, Albuquerque, New Mexico 87131, USA

⁶School of Nuclear Science and Engineering, Oregon State University, Corvallis, Oregon 97330, USA

^{a)}Author to whom correspondence should be addressed: mgenk@unm.edu

ABSTRACT

The effects of irradiation on 3C-silicon carbide (SiC) and amorphous SiC (a-SiC) are investigated using both *in situ* transmission electron microscopy (TEM) and complementary molecular dynamics (MD) simulations. The single ion strikes identified in the *in situ* TEM irradiation experiments, utilizing a 1.7 MeV Au³⁺ ion beam with nanosecond resolution, are contrasted to MD simulation results of the defect cascades produced by 10–100 keV Si primary knock-on atoms (PKAs). The MD simulations also investigated defect structures that could possibly be responsible for the observed strain fields produced by single ion strikes in the TEM ion beam irradiation experiments. Both MD simulations and *in situ* TEM experiments show evidence of radiation damage in 3C-SiC but none in a-SiC. Selected area electron diffraction patterns, based on the results of MD simulations and *in situ* TEM irradiation experiments, show no evidence of structural changes in either 3C-SiC or a-SiC.

Published under license by AIP Publishing. <https://doi.org/10.1063/1.5085216>

I. INTRODUCTION

Developing and validating multiscale predictive models for investigating irradiation effects in materials is at the forefront of materials science and engineering. Among materials of interest is silicon carbide (SiC). This high temperature and strong material is of interest in many applications, which include spacecraft structures, fuel cladding in current and next-generation light water reactors (LWRs),^{1,2} radiation-hard electronics,^{3,4} and plasma-facing blankets in fusion reactors.^{5,6} Furthermore, SiC and SiC fiber-reinforced composites are favored and widely considered for space, aerospace, and terrestrial applications because of their light-weight, low activation under neutron irradiation, good thermal and mechanical properties, and chemical stability in high temperature and oxidizing environments.⁵ SiC is also being investigated as an alternative cladding for accident tolerant fuel systems and as a protective coating of the zircaloy cladding in light water reactors (LWRs) to delay and decrease oxidation and the production of hydrogen in severe accidents.^{7–11}

Amorphous SiC (a-SiC) is also being considered as a coating for the zircaloy cladding in LWRs to suppress low temperature hydrogen corrosion and oxygen embrittlement during nominal reactor operation owing to the absence of grain boundaries. The atomic oxygen and hydrogen are produced during reactor nominal operation by the radiological dissociation of the water coolant. In addition, the lack of structure confers radiation resistance of an amorphous coating that could effectively suppress the exothermic oxidation of the underlying zircaloy cladding and the associated production of hydrogen. Therefore, it is desirable to investigate and contrast the radiation damage in both 3C-SiC and a-SiC to help develop predictive models for estimating the irradiation-induced changes in the properties of these materials.

Radiation effects in SiC have been widely investigated using in-pile neutron irradiation tests^{12,13} and electron and ion beam irradiation experiments with both *in situ* and *ex situ* transmission electron microscopy (TEM).^{9,14–20} Many of the ion beam irradiation experiments employed different ion species, different temperatures,

and varying microstructures. However, the reported results are an assortment of data points without a cohesive narrative to describe irradiation effects in SiC. In fact, the reported dose values for the amorphization of SiC at 300 K vary by more than an order of magnitude.^{15,16}

Jamison *et al.*¹⁴ compiled much of the published information and, in addition to carrying out extensive ion beam irradiation tests, have explained some of the differences in the reported results of the radiation effects in SiC. They have also pointed out several seeming contradictions in the literature. In addition, the dose-to-amorphization and whether nc-SiC is more or less radiation hard than μ c-SiC might be attributed to experimental uncertainties and/or methods used. Examples are the differences in the irradiating ion species, the specimen's microstructure (such as grain texture, refinement, and the presence of stacking faults), and the method of observation (*in situ* vs *ex situ* TEM).¹⁴ An extensive review of published data⁹ shows that predicting consistent irradiation effects in SiC is challenging, making it difficult to develop predictive models.

Liu *et al.*²¹ have irradiated SiC with a 1 MeV Kr ion beam at 800 °C and found that 2/3 of the produced defect clusters were less than 1 nm in diameter. These clusters were observable using advanced scanning transmission electron microscopy (STEM). Their cluster dynamics (CD) simulations, based on prior models of point defect production, clustering, and annihilation, were unable to reproduce the defect density distribution observed in their experiments. They were, however, able to improve the agreement between the predictions of the CD models and the experimental results by accounting for other effects, such as irradiation-induced mobility of clusters, intracascade cluster production, and the differences in the morphologies of various defect clusters.

The study by Katoh *et al.*²² can only account for 10%–45% of macroscopically measured swelling based on the produced defect clusters and loops visible with TEM. This is because many of the defects are too small to observe due to resolution limitations. The remainder of the produced defects is assumed to be small interstitial clusters, since vacancies in SiC are immobile until the temperature reaches ≈ 1273 – 1473 K.^{7,23} Even with STEM, the exact nature of the irradiation produced defects is impossible to determine. Thus, using computational models in conjunction with experiments could help assess radiation effects at time scales and resolution not possible with TEM.

A popular computational tool for quantifying the radiation damage in materials is the Stopping and Ranges of Ions in Matter (SRIM).²⁴ This Monte Carlo-based code is often used to estimate the radiation-induced average displacements per atom (dpa) in ion beam experiments. MD simulations are another computational tool for investigating radiation effects, including the production of large defects.^{25–29} MD simulations track the production of radiation damage cascades in crystalline materials with attosecond resolution and account for thermal recombination, defect clustering, and potential amorphization. These simulations employ potentials to model atomic interactions. The selected interatomic potentials, however, need to accurately reproduce the density functional theory (DFT) formation energies and the experimental results for the equations of state and defect production.^{30–32} Several potentials have been developed to model SiC,^{27,33–41} but the generally

accepted one for modeling irradiation effects in 3C-SiC is the Tersoff + ZBL potential.³³ This is despite the fact that this potential overestimates the carbon interstitial migration energy when compared to density functional theory (DFT) results. The Tersoff + ZBL potential has recently been used to simulate the production of defect cascades and estimate the threshold displacement energies (TDEs) for 3C-SiC.^{26,29,33–36,42,43} The TDEs for both C and Si primary knock-on atoms (PKAs) in SiC are highly anisotropic,^{39,44} which makes it difficult to choose a single input value into SRIM. However, recent studies^{44–46} have shown that the TDEs with 50% probability for a PKA displacement are in general agreement with the experimental values and, thus, suitable for SRIM calculations.

Although investigations of a radiation damage in ceramics using MD simulations are typically limited to a few to tens of kiloelectron volt PKAs,^{25,26,47–49} several studies of radiation effects in 3C-SiC with high-energy PKAs have been reported.^{26,29,43,49–51} One study²⁸ used MD simulations to investigate the radiation damage with 10 keV Si and Au²⁺ projectiles and compared the results to those of *in situ* TEM experiments performed in the 3.4 MeV tandem accelerator facility at the Pacific Northwest National Laboratory (PNNL). A higher disordering occurred using the Au²⁺, rather than the Si PKAs, and the Au projectiles were more likely to cause amorphization and larger defect clusters.

Other studies have investigated the defect production and clustering with up to 50 keV PKAs.^{26,49,51,52} However, the cutoff to identify the defect clusters varied between studies. For example, Gao *et al.*⁵¹ used the first nearest neighbor, Liu and Szlufarska⁴⁹ used the second nearest neighbor, and Samolyuk *et al.*²⁶ used the lattice parameter. Defect clustering was not significant in any of these studies, as the largest clusters did not exceed tens of defects. Results of Liu and Szlufarska⁴⁹ showed that the clusters had 30%–100% carbon vacancies and 60%–100% carbon interstitials. Results of Gao *et al.*⁵¹ showed that the largest cluster did not exceed 4 interstitials due to the short lifetime of the thermal spike phase, which prevented short-range diffusion and clustering. Similar behavior is observed under neutron irradiation.⁵³ The results from all these studies^{31,59,61} showed that the 50 keV PKAs produced dispersed sub-cascades, and the defects were spread out across the entire simulation domain. In metals, clustered interstitials are thermally stable and can be absorbed in grain boundaries and dislocations.⁵⁴ The absence of this type of defect production in 3C-SiC could affect the evolution of the cascade over longer time scales.

While irradiation effects in SiC have been extensively investigated using both experimental and computational methods, it is difficult to make direct comparisons due to differences in temporal resolution. The different time scales make it challenging to directly compare a single ion strike observed using TEM with that produced using MD. Nonetheless, a direct comparison would help provide confidence in the simulations. Therefore, a primary focus of this work is to identify single ion strikes in SiC using *in situ* TEM ion beam irradiation experiments with 1.7 MeV Au³⁺ ions. The results can then be compared to those of MD simulations based on the selected area electron diffraction (SAED) patterns, changes in morphology, and apparent radiation damage produced using Si PKAs up to 100 keV. To verify the soundness of the MD simulations, results of Si PKAs with energies ≤ 50 keV are first compared to prior work.

II. ION BEAM IRRADIATION EXPERIMENTS

For the *in situ* TEM irradiation experiments, a-SiC samples are deposited onto single crystal pure Si TEM windows using a 99.5% pure SiC sputtering target and the Direct Current (DC) ATC 1800 Magnetron Sputtering System at the Center for Integrated Nanotechnologies at Los Alamos National Laboratory. The base pressure in the sputtering chamber was 5.0×10^{-8} Torr ($\sim 6.67 \times 10^{-6}$ Pa), while the working pressure was 3×10^{-3} Torr (~ 0.40 Pa). During deposition, the partial pressure of the inert Argon gas in the sputtering chamber was 30 sccm, the substrate temperature was 700 °C, the DC Power was 300 W, and the distance between the target and substrate was ≈ 50 cm. At a rate of 0.93 Å/s, the SiC was deposited for 430 s to obtain a nominal film thickness of ≈ 40 nm. SAED patterns confirmed that these samples are amorphous SiC (Fig. 1).

Following deposition, some of the a-SiC specimens were annealed for 4 h at 1200 °C in a vacuum furnace at Sandia National Laboratories to form a porous, polycrystalline 3C-SiC (Fig. 2). No 4H, 6H, or any other phases were observed during SAED characterization. Subsequently, the samples were irradiated with a 1.7 MeV Au³⁺ ion beam in the JEOL 2100 TEM for 15 min in the *in situ* ion irradiation TEM (I³TEM) facility at Sandia National Laboratories.⁵⁵ The total fluence at an average flux of 3.18×10^{11} ions/cm² s was 2.87×10^{14} ions/cm², which corresponds to an average dose of 0.55 dpa in the top 40 nm of the 3C-SiC specimen and 0.995 dpa in the top 40 nm of the a-SiC specimen.

These dose values are calculated with SRIM using inputs based on the recommendations by Stoller *et al.*⁵⁶ and recommended estimates of the TDEs⁴⁴ (26 and 48 eV for carbon and silicon atoms in 3C-SiC and 13 and 27 eV in a-SiC). These TDEs correspond to a 50% displacement probability.⁴⁶ In the irradiation

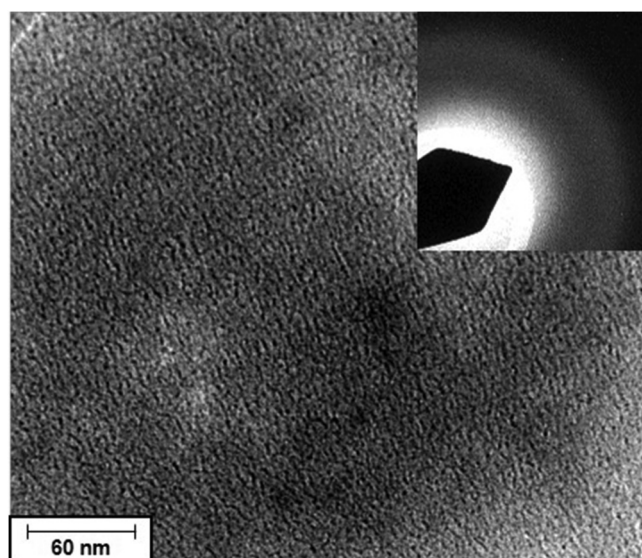


FIG. 1. Bright-field image and SAED pattern of unirradiated a-SiC.

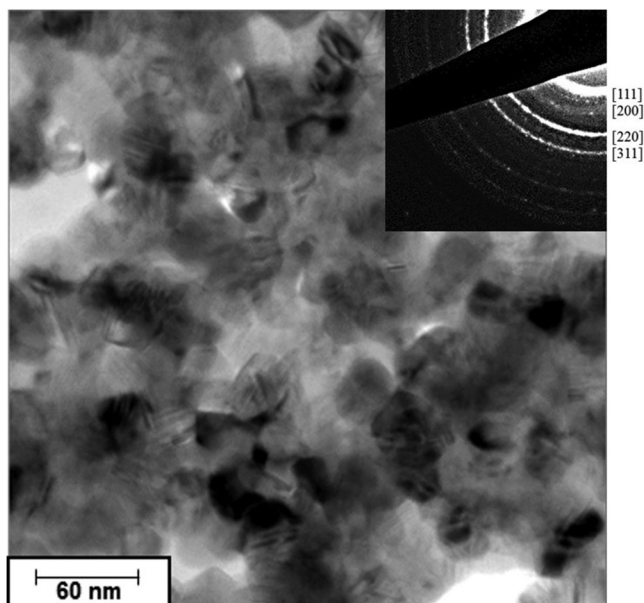


FIG. 2. Bright-field image and SAED pattern of unirradiated, sputter deposited, porous, nanocrystalline 3C-SiC.

experiments, the TEM was operated at 200 kV, while the bright-field video data were recorded *in situ* and SAED patterns were collected periodically.

III. MOLECULAR DYNAMICS SIMULATIONS

The present MD simulations for investigating radiation damage in 3C-SiC and a-SiC with Si PKAs of different energies (10–100 keV) are carried out using the Large-scale Atomic/Molecular Massively Parallel Simulator (LAMMPS),⁵⁷ in conjunction with the Tersoff + ZBL³³ potential. Performing MD simulations of 1.7 MeV Au³⁺ ions to match the *in situ* TEM experiments would be computationally prohibitive. However, using a PKA with a fraction of the Au³⁺ projectile energy is more tractable. SRIM is used to estimate the spectrum of Si PKA energies as a function of depth of the 1.7 MeV Au³⁺ ions. The most probable PKA energy is 43.6 keV, depending on the penetrating depth of the Au ions. Thus, the performed MD simulations employed Si PKAs with energies ranging from 10 to 100 keV to possibly identify a representative sampling of the likely Si PKA energies induced by 1.7 MeV Au³⁺ ions. It is important to note that since MD simulations solely account for elastic collisions and neglect the PKA energy loss due to electronic stopping, the corresponding PKA energies in the experiments would be higher.^{49,51}

Accounting for electronic stopping in MD simulations is a subject of an ongoing discussion and consideration. Including the interactions of the atomic and electronic sublattices in the MD simulation is challenging. A proposed method to account for electronic stopping in MD simulations is to add a friction term to reduce the energy of the PKAs. This method, however, precludes

communication between the electronic sublattice and the atomic lattice. Additionally, the selection of the friction term is somewhat arbitrary, especially since the stopping power does not scale linearly with PKA energy.⁵⁸ Another approach is to use the two-temperature model (TTM) in LAMMPS, which accounts for the heat transfer between the electronic and atomic subsystems. However, obtaining the initial parameters needed for this model would require extensive density functional theory (DFT) calculations, which is outside the scope of this paper.

To ensure that the produced defect cascades in the present MD simulations do not reach the periodic boundaries,⁵¹ the performed MD simulations employed significantly large system sizes, which are increased commensurate with increased PKA energy. The simulations with 10, 20, 30, 40, 50, and 60 keV Si PKAs used a system of 64×10^6 atoms, and the simulations with the 100 keV Si PKA, in the [100] crystallographic direction, used a system of 512×10^6 atoms (Table I). It is noteworthy that the number of atoms in the MD simulations with 100 keV Si PKA is more than an order of magnitude higher than previously used in reported MD simulations with 50 keV PKAs.^{26,27,49} For PKA energies of 10–60 keV, 3–4 simulation cascades are performed to improve the statistics of the results. However, for the 100 keV Si PKA, only a single simulation is carried out, due to computational limitations. Although a single simulation is clearly not indicative of average radiation effects since the damage process can be vastly different from one case to another, the obtained results provide some indication of the nature of the interaction of the 100 keV Si PKA in 3C-SiC.

The system of atoms for the MD simulations in 3C-SiC is first equilibrated in an isothermal-isobaric ensemble (NPT) at 300 K and 0 atm for 30 ps. Subsequently, it is equilibrated for 30 ps in a microcanonical ensemble (NVE). Figure 3 shows that the potential energy of the system of atoms during equilibration has fully converged, except for statistical fluctuations. Throughout the entire cascade event, a thermostatic boundary layer is applied at the boundaries of the system to readily dissipate the heat deposited by the radiation event.

The a-SiC is prepared by first equilibrating at 300 K and 0 atm for 30 ps in an NPT ensemble. Subsequently, the system of atoms is heated from 300 K to 6000 K over 10 ps and kept at 6000 K for 100 ps. The system is then quenched from 6000 K to 300 K over a period of 100 ps, equivalent to a rate of 5.7×10^{13} K/s. The resulting

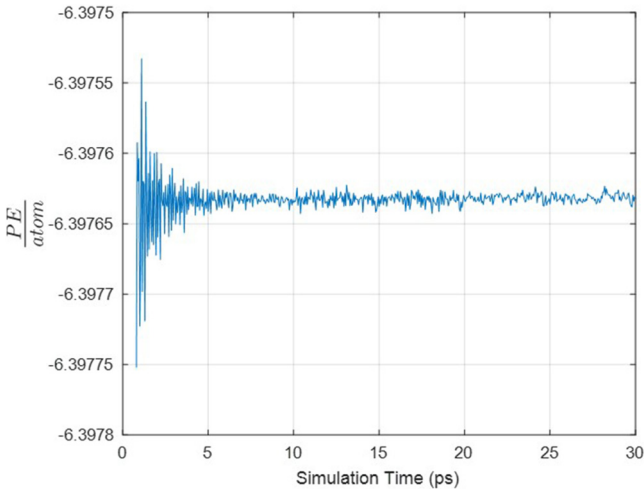


FIG. 3. Convergence of the potential energy during NPT equilibration.

system is allowed to equilibrate for 500 ps in an NPT ensemble, before initiating the radiation damage events. The performed MD simulations for 3C-SiC and a-SiC used a variable time step, with no atom moving more than 0.005 Å in a single time step.

Radiation damage simulations of high energy PKAs are typically limited to high-index directions, since channeling of the PKA can often be properly mitigated and the cascade remain within the confines of the simulation cell. In the present work, the [100] crystallographic direction is investigated since it allows the high-energy PKA to immediately lose a significant amount of energy upon colliding with its nearest neighbor. While channeling does occur, especially for the higher energy PKAs, the simulation size chosen of up to 512 000 000 atoms was large enough to contain the 100 keV Si PKA.

This work used Wigner-Seitz (WS) defect analysis to determine the number of vacancies, interstitials, and antisites, and cluster analysis to identify the clusters of vacancies (voids) and interstitials in 3C-SiC.²⁶ The lattice parameter is used to determine which defects belong to the same cluster. Simulated selected area electron diffraction (SAED) patterns of the unirradiated 3C-SiC crystal and of the radiation damaged region are generated by calculating the electron diffraction intensity on a mesh of reciprocal lattice nodes.⁵⁹ The visualization of the SAED patterns was possible using the logarithm of the diffraction intensity in Paraview.⁶⁰

IV. RESULTS AND DISCUSSION

This section presents the results of the *in situ* TEM ion beam irradiation with 1.7 MeV Au³⁺ ions. Results of the MD simulations of defect production in 3C-SiC by Si PKAs with energies up to 100 keV are also presented. Note that PKA energies ≤ 50 keV have been extensively investigated previously in SiC, thus present results in this energy range are used to validate the current simulations. Then, the energy is extended up to 100 keV, which has not been previously investigated in other studies.

TABLE I. Listing of the PKA energies and system sizes used in prior MD studies compared to the present work.

Reference	PKA energies (keV)	Atoms used	System dimensions (lattice unit)
Gao <i>et al.</i>	0.25–50	8000–6 040 000	$10 \times 10 \times 10$ – $60 \times 60 \times 210$
Liu <i>et al.</i>	0.01–50	101 376–16 252 928	$24 \times 24 \times 22$ – $128 \times 128 \times 124$
Samolyuk <i>et al.</i>	10, 50	409 600–22 070 021	$80 \times 80 \times 80$ – $150 \times 150 \times 150$
Present work	10–60	64 000 000	$200 \times 200 \times 200$
Present work	100	512 000 000	$400 \times 400 \times 400$

In addition, the results of the MD simulations and the *in situ* TEM ion beam irradiation are compared and discussed. The MD simulation results include the number and types of residual defects produced, defect clustering, extent of defect cascade, simulated SAED patterns, and estimates of the stored energy due to residual defects. The *in situ* TEM ion beam irradiation results include bright-field images of the SiC specimens, a difference image before and after irradiation, and SAED patterns of the specimens.

A. *In situ* TEM ion beam irradiation

The *in situ* ion irradiation experiments are performed at the I³TEM facility⁵⁵ using 1.7 MeV Au³⁺ ions. Despite the significantly longer time scale compared to that of the MD simulations, the experiments provide real time observation of single ions strikes, and potential radiation damage information. The selected high energy ions in the irradiation experiments produce high cascade damage in the tilted (30°) thin film specimens, without affecting the composition, as the vast majority of ions pass through the thin specimens. The ion flux and TEM imaging conditions, separated from local bending and other global imaging changes, are optimized to facilitate direct real-time observation of single strikes. A limitation of the TEM is the low spatial and temporal resolutions for identifying point defects and small defect clusters. The spatial resolution of a few nanometers and the temporal resolution of milliseconds (ms) are much lower than those in the MD simulations, which is of angstroms and picoseconds, respectively.

The bright-field image and the inset SAED pattern in Fig. 2 confirm that the thin film specimen used in the experiment is crystalline 3C-SiC. The still images in Figs. 4(a) and 4(b) are taken from recorded sequential frames, separated by 200 ms, during the *in situ* TEM irradiation experiment. The image in Fig. 4(c) highlights an observable contrast change measuring 30 nm² (5 × 6 nm²). This strain field is due to the radiation-induced defects from a single Au³⁺ ion strike. More observable contrast changes between 200 ms frames are shown in Fig. 5. The average diameter of the 10 observed ion strikes was 3.7 ± 1.5 nm. The variance in the size of the contrast regions is likely due to different amounts of energy transfer from the incident Au³⁺ ions to the lattice atoms in the SiC

specimen (referred to as PKA in the MD simulations). There is no change in the SAED patterns of the specimen, before and after irradiation. Since the resolution of the TEM is on the order of nanometers, it is not possible to identify individual point defects or small defect clusters responsible for the strain fields observed in the bright-field images. However, the MD simulation results in Sec. IV B could be used to identify possible defect types and defect cluster types causing the contrast changes.

The SAED pattern of the irradiated a-SiC does not show any ring structure and/or sharp diffraction. During irradiation with 1.7 MeV ions of Au³⁺, no contrast changes are observed, suggesting little to no structural changes in the a-SiC.

B. Molecular dynamic simulation results

Figure 6 compares the numbers of the different types of residual defects produced in 3C-SiC in the performed MD simulations using Si PKAs with energies from 10 to 100 keV. The primary residual defects are carbon interstitials and vacancies, followed sequentially by the carbon antisites, and the silicon vacancies, antisites, and interstitials. This order of the residual defects in 3C-SiC is consistent with that reported previously for PKAs with energies up to 50 keV.²⁶ The number of the residual defects produced in the MD simulations increased linearly with the PKA energy as

$$N_d = a + m E_{PKA}(\text{keV}). \quad (1)$$

In this equation, “a” is the number of defects produced by the lowest energy PKA of 10 keV and “m” is the rate of increase of the residual defects with increased PKA energy, E_{PKA} . As shown in Fig. 6 and listed in Table II, the values of “a” and “m” depend on the type of the residual defects produced in the MD simulations.

Figure 7 compares the calculated ratios of the residual carbon to silicon interstitials, vacancies, and antisites in the present MD simulations as a function of the Si PKA energy. For the 10 keV Si PKAs, the number of the residual carbon interstitials is about 23 times that of silicon and decreases to about 10 times that of silicon with 100 keV Si PKAs. The higher carbon interstitial population is due to the high carbon interstitial migration barrier modeled with

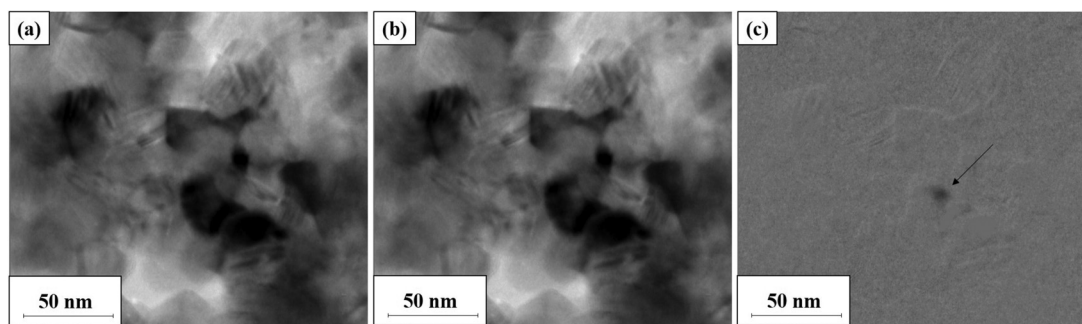


FIG. 4. (a) Bright-field micrograph of sputter deposited, porous, nanocrystalline SiC collected during *in situ* TEM ion irradiation with 1.7 MeV Au³⁺. (b) Still frame after a single observable ion strike taken from the same video, 200 ms after micrograph shown in (a). (c) Difference image comparing figures (a) and (b) to highlight the contrast changes resulting from the single ion strike (arrowed).

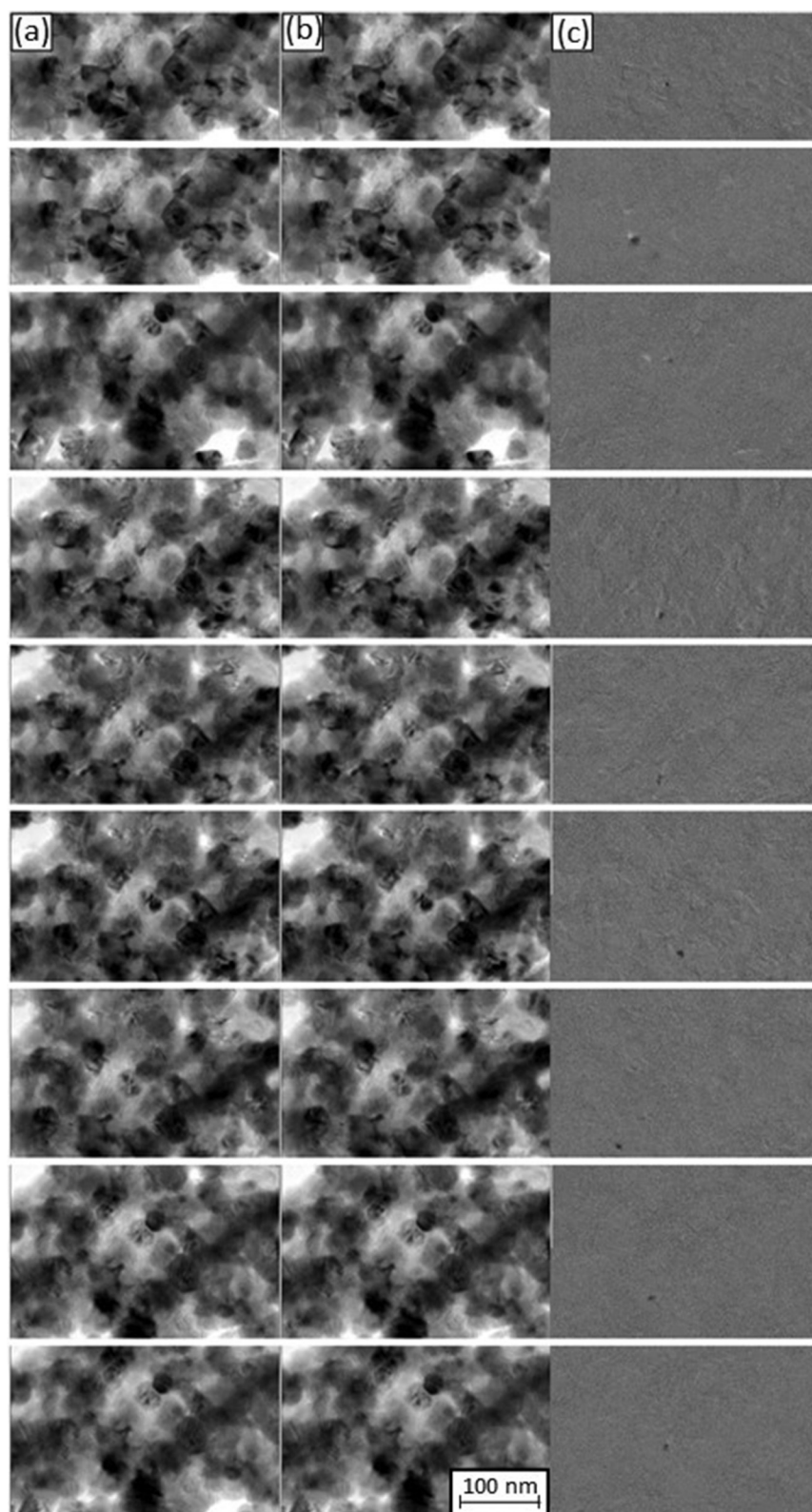


FIG. 5. (a) Bright-field micrographs of 9 ion strikes in sputter deposited, porous, nanocrystalline SiC collected during *in situ* TEM ion irradiation with 1.7 MeV Au³⁺. (b) Still frame after a single observable ion strike taken from the same video, 200 ms after micrograph shown in (a). (c) Difference image comparing figures (a) and (b) to highlight the contrast changes resulting from the single ion strike (arrowed).

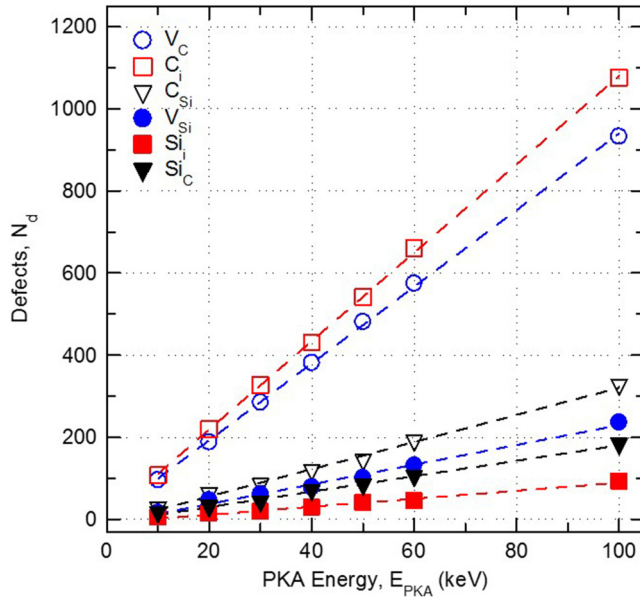


FIG. 6. Comparison of the residual number and types of defects produced in 3C-SiC with Si PKAs ranging from 10 to 100 keV.

the Tersoff + ZBL potential, which is higher than density functional theory (DFT) calculations.^{26,42} The high migration barrier suppresses recombination of the carbon interstitials that are only one lattice parameter away from a carbon vacancy.²⁶ With higher PKA energies of 100 keV, more carbon interstitials recombine due to the increase in the localized heating in and around the defect regions, due to the higher energy deposition by the PKA. The ratios of the carbon to silicon vacancies and antisites are $\approx 4\text{--}6\times$ and $\approx 1\text{--}2\times$, respectively.

Figures 8(a) and 8(b) compare the average number of produced residual clusters of vacancies and interstitials, averaged over all cascades simulated, at different Si PKA energies. As shown in Table III, the size of the largest vacancy cluster produced is $\approx 2\text{--}3$ times that of the largest interstitial cluster produced, for all cascades investigated in the present MD simulations. The number of the clusters produced, particularly the small ones, increases with increased Si PKA energy. Increasing the Si PKA energy would increase the extent of the cascade, which increases the number of the small defect clusters

TABLE II. Fitting parameters for the production of residual vacancies, interstitials, and antisites with Si PKAs of energies of 10–100 keV in 3C-SiC.

Defect	a	m
C_i	10.8	3.57
V_C	9.35	5.96
C_{Si}	3.31	-10.2
V_{Si}	2.40	-10.5
Si_C	1.88	-7.79
Si_i	0.97	-8.13

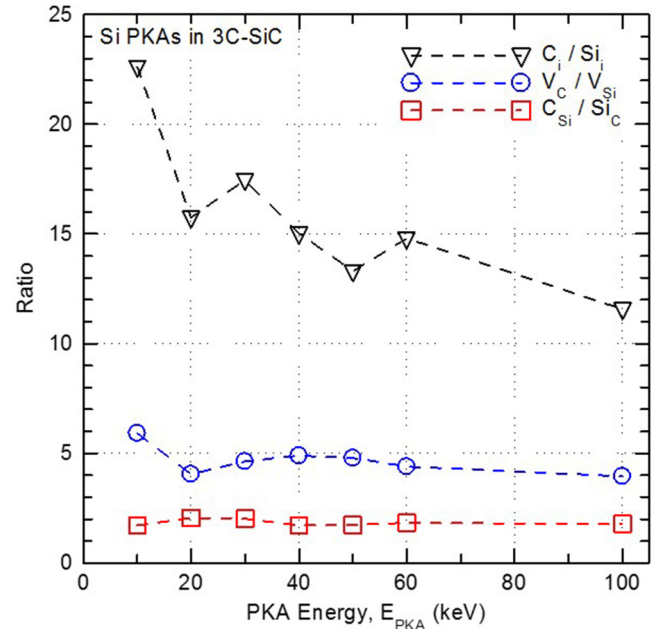


FIG. 7. Comparison of the ratios of carbon to silicon vacancies, interstitials, and antisites as a function of Si PKA energy.

produced. However, the average size of the few large clusters produced is weakly dependent on the PKA energy (Table III) due to the formation of many smaller cascades rather than increasing the number of defects in the forming clusters.

The average sizes of the largest clusters produced of residual vacancies and interstitials increase from 10.3 ± 2.1 to 30.3 ± 13.1 and from 4.0 ± 1.4 to 12.0 ± 4.4 , respectively, as the Si PKA energy increased from 10 to 40 keV, respectively. Above 40 keV, there is no clear trend observed, which could be due to subcascade splitting, a phenomenon discussed by Sand *et al.*⁶¹ Subcascade splitting refers to a change in the geometry of the cascade, shifting from a single, roughly elliptical cascade, to smaller, dispersed subcascades. Each of these dispersed subcascades has spatial access to fewer point defects per unit of incoming PKA energy. The transition from PKA energies that do not cause subcascade splitting to those that do is not necessarily sharp. In fact, Sand *et al.*⁶¹ have shown that cascades can sometimes remain intact above the subcascade splitting energy. However, the results in Fig. 9 and Table III provide supporting evidence that defect clustering is reduced for Si PKA energies >40 keV as subcascade splitting becomes a dominant factor in the evolution of the radiation damage cascade.

The clustered fraction of the interstitials produced, f_{cl}^i , which is the ratio of residual interstitials in clusters of size two or more, to the total number of the residual interstitials produced is a good measure of cluster formation. For 50 keV Si PKAs in 3C-SiC, Gao *et al.*⁵¹ reported an $f_{cl}^i = 0.28$, which is in agreement with the present work in which f_{cl}^i averages 0.26–0.33 for all cascades produced with different Si PKA energies. The calculated f_{cl}^i in the present work is almost constant for Si PKA energies from 10 to

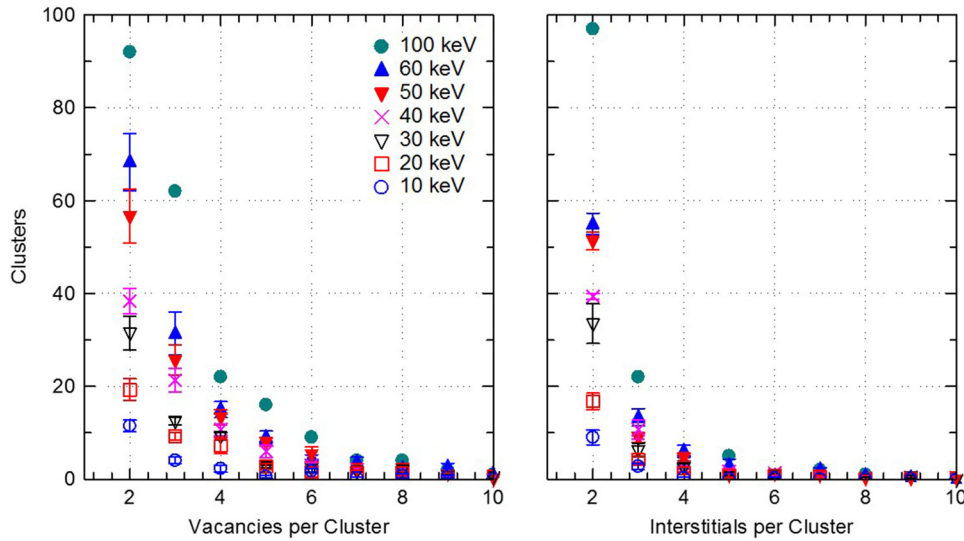


FIG. 8. Comparison of the average number and size of vacancy and interstitial clusters produced with Si PKAs of energies ranging from 10 to 100 keV in 3C-SiC.

100 keV. The calculated clustered fraction of vacancies, f_d^v , in the present work, is much higher and increases slightly from 0.67 to 0.70 as the Si PKA energy increases from 10 to 100 keV.

Figure 9 shows images of the extent of the residual defect cascades produced in the present MD simulations with 10–60 keV Si PKAs. These images are representative of multiple simulations carried out at these PKA energies. The extent of the defect cascade is defined as the distance of the furthest defect atom from the initial lattice plane of the PKA. The images in Fig. 9 show that using 64×10^6 atoms in the simulations is more than adequate to accommodate the extent of the produced cascades. The calculated average extent of the defect cascades, X (nm), is plotted in Fig. 10 vs the Si PKA energy, E_{PKA} , from 10 to 60 keV, and correlated as

$$X \text{ (nm)} = 18.1 + 4.84 E_{PKA}^{2.78}. \quad (2)$$

The penetration depth is calculated as a simple linear distance, not along the track from start to finish. The calculated total volumes of the defect regions, produced by Si PKAs, with energies from 10 to 60 keV, vary from a few to several hundred nm^3 . The extent of the

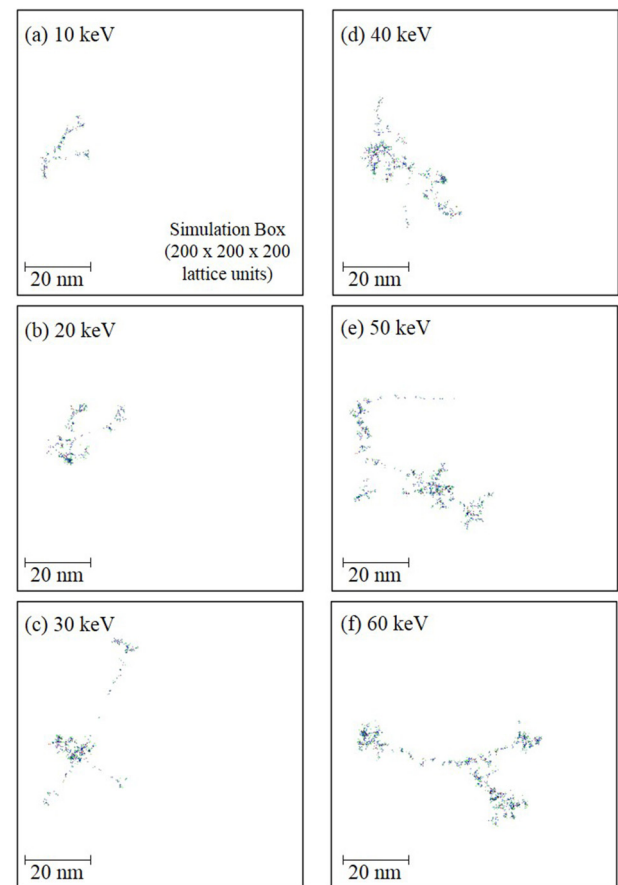


FIG. 9. Comparison of cascade penetration depth produced by Si PKAs in 3C-SiC with energies from 10 to 60 keV.

TABLE III. Comparison of the largest residual vacancy and interstitial clusters produced with Si PKAs ranging from 10 to 100 keV in 3C-SiC.

PKA energy (keV)	Average size of largest cluster	
	Vacancies	Interstitials
10	10.3 ± 2.1	4.0 ± 1.4
20	14.3 ± 7.3	6.5 ± 2.6
30	21.8 ± 4.0	11.5 ± 2.9
40	30.3 ± 13.1	12.0 ± 4.4
50	16.0 ± 3.0	8.0 ± 3.4
60	20.0 ± 2.0	8.0 ± 1.0
100	34.0	17.0

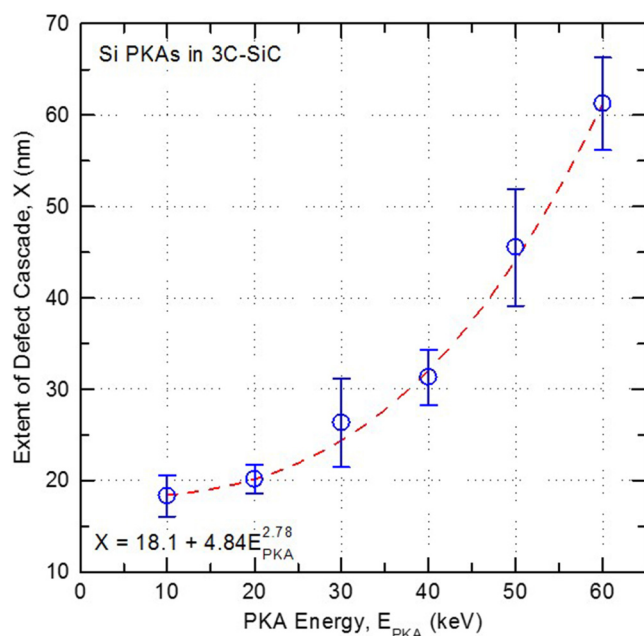


FIG. 10. Comparison of average cascade penetration depth with Si PKAs ranging from 10 to 60 keV in 3C-SiC.

defect cascade produced with the 100 keV Si PKA is not shown in Fig. 10 or included in the correlation in Eq. (2) since only a single cascade is simulated due to the limitation on time and computation requirements to run several cascades. Figure 11 presents images of the residual damage produced in the present simulation with the 100 keV Si PKA. Each of these damaged regions comprises several defect clusters in close proximity. The areas of these regions range from several to 76 nm² (Fig. 11), and the volume ranges from tens to several hundred nm³.

The absence of large defect clusters in 3C-SiC with the 100 keV Si PKA suggests that amorphous regions are unlikely to form by a single Si PKA. To confirm the retention of crystallinity in the region of the defect cascade produced by the 100 keV Si PKA, the simulated SAED patterns are obtained for three zone axes ([100], [110], and [111]) and compared to the those of unirradiated 3C-SiC (Fig. 12). It is important to note that the SAED patterns for the irradiated 3C-SiC are taken over the irradiated region and not the entire simulation domain. The SAED pattern taken over the entire 512 × 10⁶ atom system used in the simulations filters out the residual defects produced as noise.

The SAED patterns of the results of the MD simulations, using Si PKAs with energies from 10 to 100 keV, show no evidence of changes in the atomic structure in either 3C-SiC or a-SiC (Figs. 12 and 13). The stronger diffraction peaks for the unirradiated 3C-SiC are because the results are averaged over 10 ps, whereas the ones for the irradiated crystal are just a single snapshot in time. Simulated SAED patterns of the unirradiated and irradiated a-SiC with a 30 keV Si PKA (Fig. 13) show no detectable changes in the atomic structure or short-range order. This is also

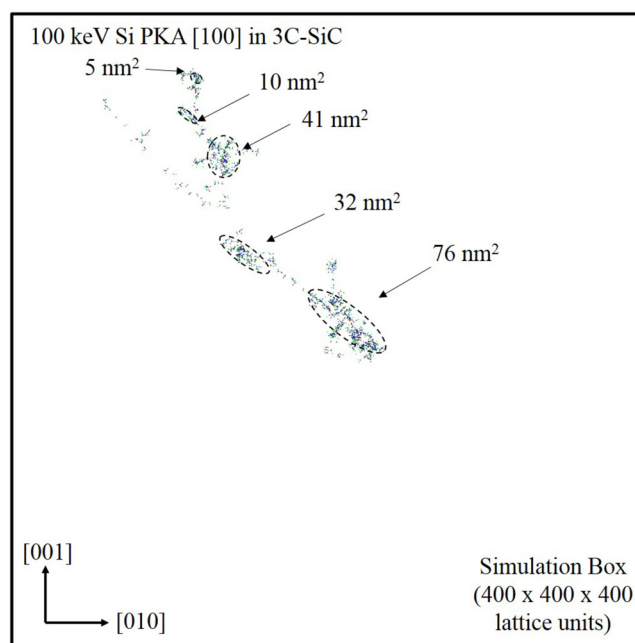


FIG. 11. Cross-sectional view of the radiation damage cascade produced by a 100 keV Si PKA in 3C-SiC.

confirmed by the radial distribution function (RDF) based on the results of the MD simulation of a-SiC with a 30 keV Si PKA (Fig. 14). The figure shows that the RDFs in a-SiC before and after irradiation are identical. Thus, the results of the SAED patterns and RDFs confirm that both 3C-SiC and a-SiC are unlikely to experience significant structural changes with a single Si PKA up to 100 keV, and up to 30 keV for a-SiC. Despite the absence of significant structural changes, energy of the PKA can be partially stored in the produced defects in the material.⁶²

Before irradiation, and once the system of atoms is fully equilibrated at 300 K, the potential energy of the entire system is calculated. After irradiation, and once the system temperature drops down to its initial value of 300 K, the potential energy is once again calculated. The difference between the values of the potential energy before and after irradiation represents the amount of stored energy due to the produced point defects and small defect clusters. They cause local stresses in the 3C-SiC, commensurating with the stored energy. In the present MD simulations at 300 K, since the produced vacancies are not mobile, they are to remain in the material until self-interstitial atoms and clusters annihilate with these vacancies. The fraction of the PKA energy that remains stored in the crystal lattice as defects is 10% for all PKA energies investigated. Unlike crystalline SiC, no detectable amount of PKA energy is stored in irradiated a-SiC. The PKA energy dissipates to the bulk material at the thermostatic boundary, suggesting that no change in morphology occurs. While atoms are more likely to be displaced in irradiated a-SiC, there is no evidence of changes in the atomic structure in the present MD simulations with Si PKAs with energies up to 30 keV. These results suggest that a-SiC is radiation tolerant and is in

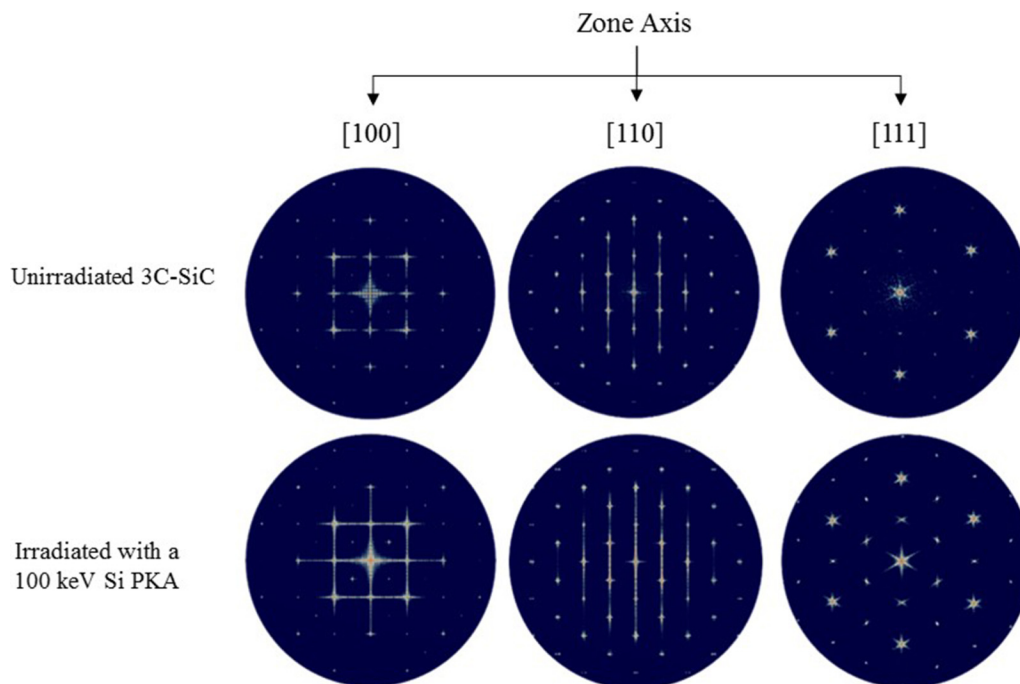


FIG. 12. Comparison of simulated SAED patterns for four zone axes of the unirradiated 3C-SiC, to the region irradiated with a 100 keV Si PKA.

agreement with those of prior work showing that amorphous SiOC alloys provide superior radiation tolerance.⁶³

C. Discussion

Several observations are made in contrasting the results of the present MD simulations using Si PKAs, with energies ranging from

10 to 100 keV in 3C-SiC, and 10 and 30 keV in a-SiC, to those of the *in situ* TEM irradiation with 1.7 MeV Au³⁺ ions. Defect production in 3C-SiC is observed both in the MD simulations and the ion beam irradiation experiments. In the *in situ* ion beam irradiation experiment, it is impossible to identify the number and distribution of the point defects causing the observed areas of contrast to change (strain fields) from the impact of single Au³⁺ ions in the

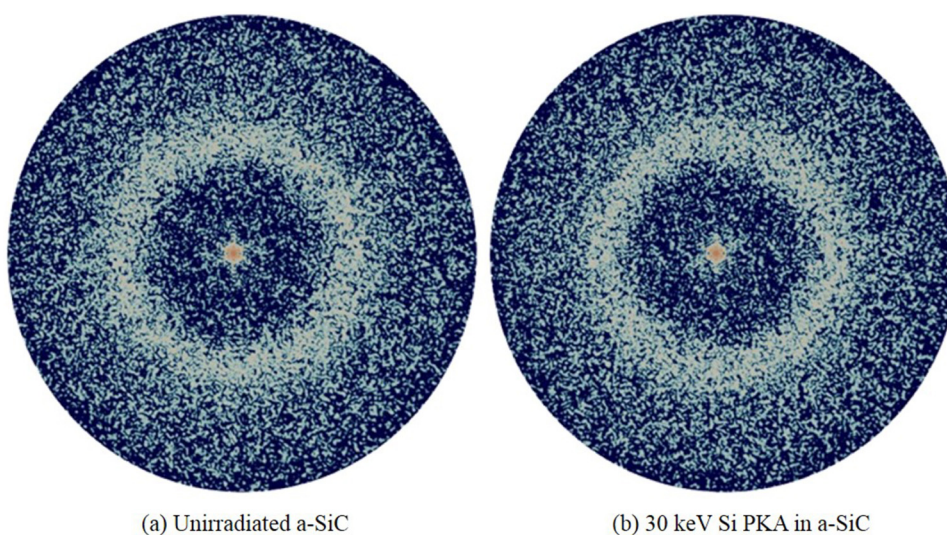


FIG. 13. Comparison of simulated SAED patterns of unirradiated a-SiC and a region of the a-SiC irradiated with a 30 keV Si PKA. (a) unirradiated a-SiC and (b) irradiated a-SiC with 30 keV Si PKA.

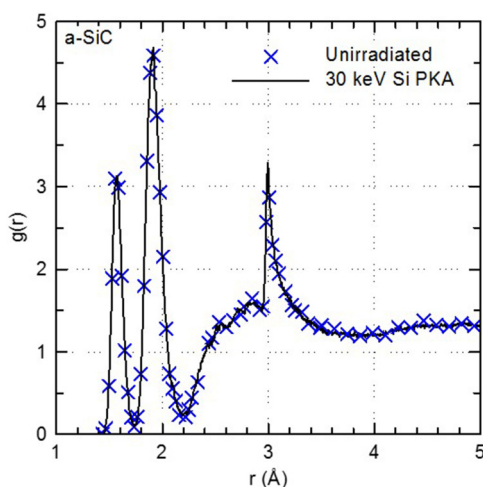


FIG. 14. Radial distribution function of a-SiC before and after irradiation with a 30 keV Si PKA.

3C-SiC. However, the MD simulation results for high energy PKAs could be used to determine the defect structures that are likely responsible for the produced strain fields. The results of the MD simulation, with a 100 keV Si PKA, show several defect regions that vary in area from 5 to 76 nm² and in volume from tens to several hundred nm³. In the experiments, the average diameter of the strain field produced by an ion strike was 3.7 ± 1.5 nm². The contrast regions from the ion beam irradiation experiment likely vary in size due to the different amounts of energy being deposited by the incident ions to a specific region of the thin film 3C-SiC specimen, which partially depend on the incident angle of the Au³⁺ ions.

The MD simulation results include the number and types of all defects produced, the size of defect clusters, and the average number of interstitials and vacancies per cluster, which is not possible to detect using modern *in situ* TEM ion beam irradiation experiments. Computational tools such as MD simulations predict changes to the crystal lattice at the atomic level within picosecond time scales, while *in situ* TEM irradiation can be used to observe radiation effects within millisecond time scales. The evolution of radiation damage cascades in 3C-SiC beyond a nanosecond to a millisecond is still not well understood and is the subject of extensive investigation at the present time.^{21,49,64}

The present results of the MD simulations and *in situ* TEM irradiation also show no evidence of observable radiation damage in a-SiC, despite the much lower TDEs for PKA displacement than in 3C-SiC.⁴⁴ The changes in the total potential energy of the atom system in the MD simulations of a-SiC is undetectable, compared as much as 10% of the total system energy due to the produced residual defects in the 3C-SiC.

V. SUMMARY AND CONCLUSIONS

MD simulations and complementary *in situ* TEM Au³⁺ ion beam irradiation are performed to assess radiation effects in

3C-SiC and a-SiC. The MD simulations with Si PKAs of energies ranging from 10 to 100 keV investigated the production of residual point defects and defect clusters. Sequential bright-field images of ion beam irradiation helped identify contrast changes in the irradiated regions, and SAED patterns helped detect the changes in the microstructure before and after irradiation. Due to the difference in the time scale for the MD simulations and the *in situ* TEM irradiation, different but complementary information is obtained.

MD simulation results confirm that carbon vacancies and interstitials are the primary residual point defects in 3C-SiC, while the clustering and the extent of the defect cascades depend on the Si PKA energy. The largest clusters increase in size from 10.3 ± 2.1 to 30.3 ± 13.1 vacancies and from 4.0 ± 1.4 to 12.0 ± 4.4 interstitials, respectively, as the Si PKA energy increases from 10 to 40 keV. Beyond 40 keV, the formation of clusters is more random and extends over a large region of the simulation domain. Generally, the size of the largest vacancy cluster is ≈ 2 to 3 times that of the largest interstitial cluster for all Si PKA energies investigated. The retention of 3C-SiC crystallinity is confirmed by the SAED patterns before and after irradiation using both MD simulations and *in situ* TEM irradiation. These patterns also confirmed the lack of changes in a-SiC after irradiation.

The change in the stored energy in the irradiated 3C-SiC due to point defects and defect clusters is estimated to be $\approx 10\%$ of all energies of the Si PKAs, while that in the irradiated a-SiC is undetectable. The radiation tolerance of a-SiC is also confirmed by the SAED patterns of the results of the MD simulations and the *in situ* TEM irradiation experiments using Au³⁺ ions.

In conclusion, the combined theoretical and experimental approach of using MD simulations and *in situ* TEM experiments provides valuable information on the effect of irradiation in 3C-SiC and a-SiC. This information is useful to current and future consideration of using these materials in developing accident tolerant fuel systems for the present fleet and next-generation LWRs, as well as in the plasma-facing blankets in fusion reactors. The radiation hardness of a-SiC, combined with the absence of grain boundaries, makes it a promising protective coating for metal and metal-alloy structures for operating in harsh environments combining high temperature and radiation.

ACKNOWLEDGMENTS

This research, funded by the Institute for Space and Nuclear Power Studies, is performed, in part, at the Center for Integrated Nanotechnologies, an Office of Science User Facility operated for the U.S. Department of Energy (DOE) Office of Science and used the resources of the High Performance Computing Center at Idaho National Laboratory, which is supported by the Office of Nuclear Energy of the U.S. Department of Energy and the Nuclear Science User Facilities under Contract No. DEAC0705ID14517, and at the Center for Advanced Research Computing, supported in part by the National Science Foundation (NSF), for providing high performance computing and large-scale storage.

We greatly appreciate the valuable support and assistance provided by Mr. Kevin Baldwin at LANL for performing the thin film deposition samples, and by Dr. Caitlin Taylor for their time and guidance in using the ion beam at the TEM irradiation facility, help

with the interpretation of the results, and the discussion, review comments, and feedback.

Los Alamos National Laboratory, an affirmative action equal opportunity employer, is operated by the Los Alamos National Security, LLC, for the National Nuclear Security Administration of the U.S. Department of Energy under Contract No. DE-AC52-06NA25396.

Sandia National Laboratories is a multimission laboratory managed and operated by the National Technology and Engineering Solutions of Sandia, LLC, a wholly owned subsidiary of Honeywell International, Inc., for the U.S. DOE's National Nuclear Security Administration under Contract No. DE-NA-0003525. The views expressed in the article do not necessarily represent the views of the U.S. DOE or the United States Government.

REFERENCES

- ¹R. A. Coward, C. R. Winkler, W. A. Hanson, M. L. Jablonski, and M. L. Taheri, *J. Nucl. Mater.* **457**, 298 (2015).
- ²K. Murty and I. Charit, *J. Nucl. Mater.* **383**, 189 (2008).
- ³L. B. B. Aji, J. B. Wallace, and S. O. Kucheyev, *Sci. Rep.* **7**, 44703 (2017).
- ⁴A. Fissel, *Phys. Rep.* **379**, 149 (2003).
- ⁵A. Ivekovic, S. Novak, G. Drazic, D. Blagoeva, and S. G. de Vicente, *J. Eur. Ceram. Soc.* **33**, 1577 (2013).
- ⁶Y.-H. Yun, Y.-H. Park, M.-Y. Ahn, and S. Cho, *Ceram. Int.* **40**, 879 (2014).
- ⁷Y. Katoh, L. L. Snead, I. Szlufarska, and W. J. Weber, *Curr. Opin. Solid State Mater. Sci.* **16**, 143 (2012).
- ⁸Y. Katoh and K. A. Terrani, ORNL/TM-2015/454, Oak Ridge National Laboratory, 2015.
- ⁹Y. Zhang, M. Ishimaru, T. Varga, T. Oda, C. Hardiman, H. Xue, Y. Katoh, S. Shannon, and W. J. Weber, *Phys. Chem. Chem. Phys.* **14**, 13429 (2012).
- ¹⁰S. J. Zinkle, K. A. Terrani, J. C. Gehin, L. J. Ott, and L. L. Snead, *J. Nucl. Mater.* **448**, 374 (2014).
- ¹¹C. P. Deck, G. M. Jacobsen, J. Sheeder, O. Gutierrez, J. Zhang, J. Stone, H. E. Khalifa, and C. A. Back, *J. Nucl. Mater.* **466**, 667 (2015).
- ¹²Y. Katoh, K. Ozawa, C. Shih, T. Nozawa, R. J. Shinavski, A. Hasegawa, and L. L. Snead, *J. Nucl. Mater.* **448**, 448 (2014).
- ¹³L. L. Snead, K. A. Terrani, Y. Katoh, C. Silva, K. J. Leonard, and A. G. Perez-Bergquist, *J. Nucl. Mater.* **448**, 389 (2014).
- ¹⁴L. Jamison, K. Sridharan, S. Shannon, and I. Szlufarska, *J. Mater. Res.* **29**, 2871 (2014).
- ¹⁵L. Jamison, M.-J. Zheng, S. Shannon, T. Allen, D. Morgan, and I. Szlufarska, *J. Nucl. Mater.* **445**, 181 (2014).
- ¹⁶W. Jiang, H. Wang, I. Kim, Y. Zhang, and W. J. Weber, *J. Mater. Res.* **25**, 2341 (2010).
- ¹⁷W. Jiang, H. Wang, I. Kim, I. T. Bae, G. Li, P. Nachimuthu, Z. Zhu, Y. Zhang, and W. J. Weber, *Phys. Rev. B* **80**, 161301 (2009).
- ¹⁸L. Jamison, P. Xu, K. Sridharan, and T. Allen, "Radiation resistance of nanocrystalline silicon carbide," in *Advances in Materials Science for Environmental and Nuclear Technology II-Materials Science and Technology 2010 Conference and Exhibition, MS and T'10* (John Wiley & Sons, Inc., Hoboken, New Jersey, 2011), p. 161.
- ¹⁹H. Inui, H. Mori, and H. Fujita, *Philos. Mag. B* **61**, 107 (1990).
- ²⁰H. Inui, H. Mori, A. Suzuki, and H. Fujita, *Philos. Mag. B* **65**, 1 (1992).
- ²¹C. Liu, L. He, Y. Zhai, B. Tyburska-Püschel, P. Voyles, K. Sridharan, D. Morgan, and I. Szlufarska, *Acta Mater.* **125**, 377 (2017).
- ²²Y. Katoh, L. Snead, and S. Golubov, "Analyzing irradiation-induced creep of silicon carbide," in *Mech. Prop. Perform. Eng. Ceram. Compos. III* **28.2** (John Wiley & Sons, Inc., Hoboken, New Jersey, 2007), pp. 297–305.
- ²³W. E. Carlos, N. Y. Garces, E. R. Glaser, and M. A. Fanton, *Phys. Rev. B* **74**, 235201 (2006).
- ²⁴J. F. Ziegler and J. P. Biersack, "The stopping and range of ions in matter," in *Treatise on Heavy-Ion Science* (Springer, Boston, MA, 1985), pp. 93–129.
- ²⁵B. J. Cowen and M. S. El-Genk, *Model. Simul. Mater. Sci.* **25**, 055001 (2017).
- ²⁶G. D. Samolyuk, Y. N. Osetsky, and R. E. Stoller, *J. Nucl. Mater.* **465**, 83 (2015).
- ²⁷F. Gao and W. J. Weber, *Phys. Rev. B* **63**, 054101 (2000).
- ²⁸F. Gao, W. J. Weber, and W. Jiang, *Phys. Rev. B* **63**, 214106 (2001).
- ²⁹D. E. Farrell, N. Bernstein, and W. K. Liu, *J. Nucl. Mater.* **385**, 572 (2009).
- ³⁰B. J. Cowen and M. S. El-Genk, *Comput. Mater. Sci.* **111**, 269 (2016).
- ³¹B. J. Cowen and M. S. El-Genk, *Comput. Mater. Sci.* **107**, 88 (2015).
- ³²M. S. El-Genk, K. Talaat, and B. J. Cowen, *J. Appl. Phys.* **123**, 205104 (2018).
- ³³R. Devanathan, T. D. de la Rubia, and W. J. Weber, *J. Nucl. Mater.* **253**, 47 (1998).
- ³⁴R. Devanathan and W. J. Weber, *J. Nucl. Mater.* **278**, 258 (2000).
- ³⁵J. M. Perlado, L. Malerba, A. Sanchez-Rubio, and T. D. de la Rubia, *J. Nucl. Mater.* **276**, 235 (2000).
- ³⁶L. Malerba and J. M. Perlado, *Phys. Rev. B* **65**, 045202 (2002).
- ³⁷J. M. Perlado, *J. Nucl. Mater.* **251**, 98 (1997).
- ³⁸W. Windl, T. J. Lenosky, J. D. Kress, and A. F. Voter, *Nucl. Instrum. Methods Phys. Res. B* **141**, 61 (1998).
- ³⁹G. Lucas and L. Pizzagalli, *Nucl. Instrum. Methods Phys. Res. B* **229**, 359 (2005).
- ⁴⁰A. A. Demkov, J. Ortega, O. F. Sankey, and M. P. Grumbach, *Phys. Rev. B* **52**, 1618 (1995).
- ⁴¹F. Gao, E. J. Bylaska, W. J. Weber, and L. R. Corrales, *Phys. Rev. B* **64**, 245208 (2001).
- ⁴²F. Gao and W. J. Weber, *Nucl. Instrum. Methods Phys. Res. B* **191**, 504 (2002).
- ⁴³R. Devanathan, W. Weber, and T. D. de La Rubia, *Nucl. Instrum. Methods Phys. Res. B* **141**, 118 (1998).
- ⁴⁴B. J. Cowen and M. S. El-Genk, *Comput. Mater. Sci.* **151**, 73 (2018).
- ⁴⁵B. S. Thomas, N. A. Marks, L. R. Corrales, and R. Devanathan, *Nucl. Instrum. Methods Phys. Res. B* **239**, 191 (2005).
- ⁴⁶B. J. Cowen and M. S. El-Genk, *Model. Simul. Mater. Sci.* **25**, 085009 (2017).
- ⁴⁷B. Ueberuaga, R. Smith, A. Cleave, G. Henkelman, R. Grimes, A. Voter, and K. Sickafus, *Phys. Rev. B* **71**, 104102 (2005).
- ⁴⁸K. Trachenko, E. Zarkadoulas, I. Todorov, M. Dove, D. Dunstan, and K. Nordlund, *Nucl. Instrum. Methods Phys. Res. B* **277**, 6 (2012).
- ⁴⁹C. Liu and I. Szlufarska, *J. Nucl. Mater.* **509**, 392 (2018).
- ⁵⁰N. Swaminathan, P. J. Kamenski, D. Morgan, and I. Szlufarska, *Acta Mater.* **58**, 2843 (2010).
- ⁵¹F. Gao, W. J. Weber, and R. Devanathan, *Nucl. Instrum. Methods Phys. Res. B* **180**, 176 (2001).
- ⁵²R. Devanathan, W. J. Weber, and F. Gao, *J. Appl. Phys.* **90**, 2303 (2001).
- ⁵³H. C. Huang and N. Ghoniem, *J. Nucl. Mater.* **250**, 192 (1997).
- ⁵⁴D. Bacon, F. Gao, and Y. N. Osetsky, *J. Nucl. Mater.* **276**, 1 (2000).
- ⁵⁵K. Hattar, D. C. Bufford, and D. L. Buller, *Nucl. Instrum. Methods Phys. Res. B* **338**, 56 (2014).
- ⁵⁶R. E. Stoller, M. B. Toloczko, G. S. Was, A. G. Certain, S. Dwaraknath, and F. A. Garner, *Nucl. Instrum. Methods Phys. Res. B* **310**, 75 (2013).
- ⁵⁷S. Plimpton, *J. Comput. Phys.* **117**, 1 (1995).
- ⁵⁸C.-W. Lee and A. Schleife, "Hot-electron mediated ion diffusion in semiconductors for ion-beam nanostructuring," *Nano Lett.* **19**, 3939 (2019).
- ⁵⁹S. P. Coleman, D. E. Spearot, and L. Capolungo, *Model. Simul. Mater. Sci.* **21**, 055020 (2013).
- ⁶⁰U. Ayachit, *The Paraview Guide: A Parallel Visualization Application* (Kitware, Inc., 2017).
- ⁶¹A. E. Sand, D. R. Mason, A. De Backer, X. Yi, S. L. Dudarev, and K. Nordlund, *Mater. Res. Lett.* **5**, 357 (2017).
- ⁶²I. T. Lu and M. Bernardi, *Sci. Rep.* **7**, 3403 (2017).
- ⁶³M. Nastasi, Q. Su, L. Price, J. A. C. Santana, T. Y. Chen, R. Balerio, and L. Shao, *J. Nucl. Mater.* **461**, 200 (2015).
- ⁶⁴H. Jiang, C. Jiang, D. Morgan, and I. Szlufarska, *Comp. Mater. Sci.* **89**, 182 (2014).